

# Small-scale soft-bodied robot with multimodal locomotion

Wenqi Hu<sup>1\*</sup>, Guo Zhan Lum<sup>1\*</sup>, Massimo Mastrangeli<sup>1</sup> & Metin Sitti<sup>1</sup>

**Untethered small-scale (from several millimetres down to a few micrometres in all dimensions) robots that can non-invasively access confined, enclosed spaces may enable applications in microfactories such as the construction of tissue scaffolds by robotic assembly<sup>1</sup>, in bioengineering such as single-cell manipulation and biosensing<sup>2</sup>, and in healthcare<sup>3–6</sup> such as targeted drug delivery<sup>4</sup> and minimally invasive surgery<sup>3,5</sup>.** Existing small-scale robots, however, have very limited mobility because they are unable to negotiate obstacles and changes in texture or material in unstructured environments<sup>7–13</sup>. Of these small-scale robots, soft robots have greater potential to realize high mobility via multimodal locomotion, because such machines have higher degrees of freedom than their rigid counterparts<sup>14–16</sup>. Here we demonstrate magneto-elastic soft millimetre-scale robots that can swim inside and on the surface of liquids, climb liquid menisci, roll and walk on solid surfaces, jump over obstacles, and crawl within narrow tunnels. These robots can transit reversibly between different liquid and solid terrains, as well as switch between locomotive modes. They can additionally execute pick-and-place and cargo-release tasks. We also present theoretical models to explain how the robots move. Like the large-scale robots that can be used to study locomotion<sup>17</sup>, these soft small-scale robots could be used to study soft-bodied locomotion produced by small organisms.

Our robot is constructed of soft active materials, which can be magnetically actuated to generate desired time-varying shapes<sup>16</sup> (see Supplementary Information section S1). Although our robotic system includes both an untethered soft device and the electromagnets that remotely generate the actuating fields (see Supplementary Information section S2 and Supplementary Fig. 2), we refer to only the untethered soft device as a ‘robot’, for consistency with the literature<sup>3–5,16,18,19</sup>. Unlike previous robots constructed with similar materials<sup>7,16</sup>, our proposed robot design and actuation inputs can achieve multimodal locomotion, and we have concurrently accounted for the robot’s programmed soft-bodied deformation and rigid-body rotation characteristics in different terrains. The choice of magnetic actuation suits various applications because the actuating fields can easily and harmlessly penetrate most biological and synthetic materials<sup>3,4</sup>. This work uses external (off-board) magnetic actuation only, but it should also be possible to create similar soft machines that use internal (on-board) soft actuation methods<sup>20</sup> to produce similar time-varying shapes and rotation.

The magneto-elastic, rectangular-sheet-shaped, soft robot is made of silicone elastomer (Ecoflex 00-10) embedded with hard magnetic neodymium-iron-boron (NdFeB) microparticles that have an average diameter of 5 µm. The surfaces of the robot are hydrophobic, and they can potentially be made biocompatible<sup>21</sup> (Supplementary Information section S1C). By following the magnetization process described in Supplementary Information section S1A, the robot can be programmed to have a single-wavelength harmonic magnetization profile  $\mathbf{m}$  along its body (Fig. 1a and Supplementary Fig. 1). After  $\mathbf{m}$  is programmed,

the robot can be controlled by a time-varying magnetic field  $\mathbf{B}$  to generate different modes of locomotion. Unless otherwise specified,  $\mathbf{B}$  is spatially uniform, and therefore no magnetic forces are applied to translate the robot (Supplementary Information section S15). The uniform  $\mathbf{B}$ , however, can control the robot’s morphology and steer it to move in a desired direction. To describe the effects of  $\mathbf{B}$ , we express  $\mathbf{B} = [\mathbf{B}_{xy}^T, B_z]^T$  with respect to the robot’s body frame (Fig. 1a) where  $\mathbf{B}_{xy}$  represents the  $x$ - $y$  plane components of  $\mathbf{B}$ , that is,  $\mathbf{B}_{xy} = [B_x, B_y]^T$ . The interaction between  $\mathbf{B}_{xy}$  and  $\mathbf{m}$  produces spatially varying magnetic torques that deform the robot, and hence controlling  $\mathbf{B}_{xy}$  allows us to generate the desired time-varying shapes for the robot. As the deformed robot possesses an effective magnetic moment  $\mathbf{M}_{\text{net}}$  (Fig. 1b), which tends to align with  $\mathbf{B}$ , we can control  $B_z$  to rotate the robot about its  $y$  axis, steering it along a desired direction (see Supplementary Information section S3B(II)).

Depending on the magnitude of  $\mathbf{B}_{xy}$ —that is,  $B_{xy}$ —the robot exhibits different shape-changing mechanisms (Fig. 1b and Supplementary Information section S3A-B). When  $B_{xy}$  is small (for example,  $< 5$  mT) and  $\mathbf{B}_{xy}$  is aligned along the two principal directions shown in Fig. 1b (II and III), the prescribed  $\mathbf{m}$  produces a sine or a cosine shape for the robot. Because the robot’s deformation is small in such conditions, orienting  $\mathbf{B}_{xy}$  away from the principal directions generates a weighted superposition of the two basic configurations. Thus, we can create a travelling wave along the robot’s body by using a rotating  $\mathbf{B}_{xy}$  that has a small constant magnitude. As the robot’s  $\mathbf{M}_{\text{net}}$  is always parallel to the applied  $\mathbf{B}_{xy}$  in small-deflection conditions, the robot does not experience any rigid-body magnetic torque and consequent rotation about its  $z$  axis (Supplementary Information section S3B(I)). Conversely, when  $B_{xy}$  has high magnitude (for example,  $B_{xy} = 20$  mT) and is aligned along the principal axis shown in Fig. 1b (IV and V), the robot undergoes a large-deflection shape change, deforming into either a ‘C’- or a ‘V’-shape. However, if the direction of  $\mathbf{B}_{xy}$  is not along this principal axis, the deformed robot generates a large  $\mathbf{M}_{\text{net}}$  that is generally non-parallel to the applied field, and this makes the robot rotate about its  $z$  axis until its  $\mathbf{M}_{\text{net}}$  aligns with  $\mathbf{B}_{xy}$  (Fig. 1c and Supplementary Information section S3B(I)). At the end of this rotation, the robot will assume its ‘C’- or ‘V’-shape configuration because the generated  $\mathbf{M}_{\text{net}}$  in these configurations is naturally aligned with the applied  $\mathbf{B}_{xy}$ . Using this mechanism, we can control the robot’s angular displacement about its  $z$  axis to enable locomotion modalities like rolling, walking and jumping.

By using the steering and shape-changing mechanisms, we demonstrate all of our robot’s locomotion modes in Figs 2 and 3. When completely immersed in water, the robot can swim upwards and overcome gravity (Fig. 2a, Supplementary Video 1, and Supplementary Information section S10). A periodic  $\mathbf{B}$  with time-varying magnitude along the principal axis allows the shape of the robot to alternate between the ‘C’- and ‘V’-shapes, enacting a gait similar to jellyfish swimming<sup>22</sup>. Inertial effects at Reynolds number ranging from 74 to 190 permit this time-symmetric but speed-asymmetric swimming gait

<sup>1</sup>Physical Intelligence Department, Max Planck Institute for Intelligent Systems, 70569 Stuttgart, Germany.

\*These authors contributed equally to this work.

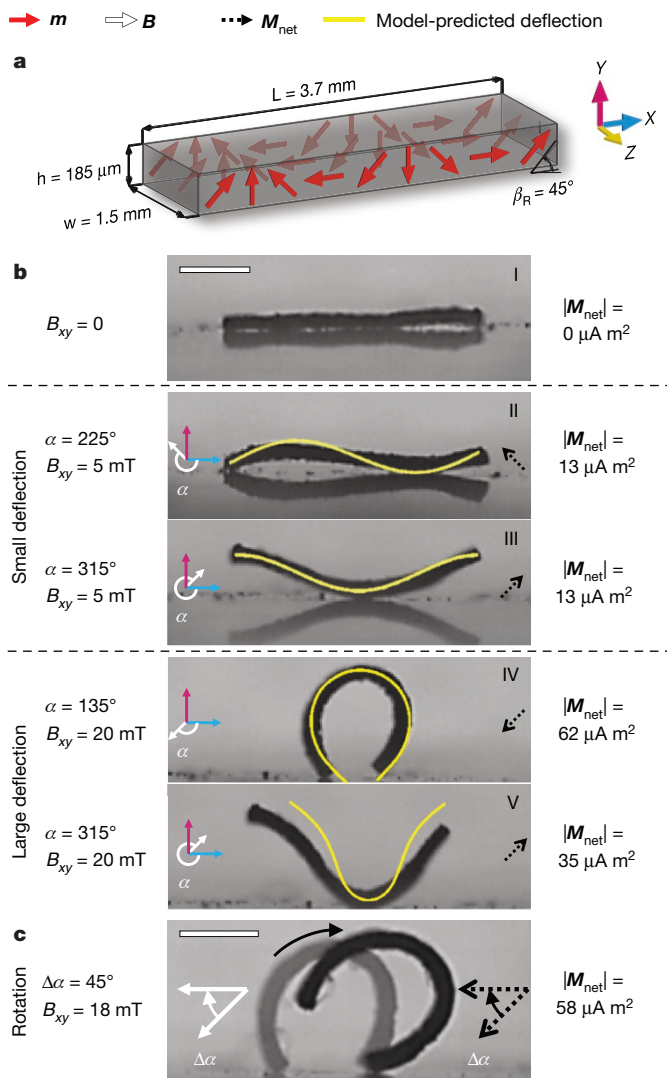


**Figure 1 | Design, shape-change mechanisms and rigid-body rotation of the magneto-elastic soft millirobot.** **a**, The rectangular-sheet-shaped magnetic soft robot's dimensions and magnetization profile  $m$ . The profile can be described as a single-wavelength harmonic function for its  $m_x$  and  $m_y$  components along the robot's length  $L$  and equally along its width  $w$  and thickness  $h$ .  $\beta_R$  is the phase shift in  $m$  that determines the principal directions (Supplementary Information section S3A). **b**, Theoretically predicted (Supplementary Information section S3A) and experimental shapes of a magnetically deformed millirobot.  $\alpha$  is a clockwise angle from the  $x$  axis, and it is used for describing the direction of  $B_{xy}$ . In (I), the robot is in its rest state under null  $B_{xy}$ . A small residual curvature is induced by the pre-stress caused by the demoulding process. (II) and (III) show small-deflection shapes under a small-magnitude  $B_{xy}$  ( $B_{xy} = 5 \text{ mT}$ ) aligned along the two principal directions ( $\alpha = 225^\circ$  for the sine shape and  $315^\circ$  for the cosine shape) in the  $x$ - $y$  plane. In contrast, the robot deforms into a 'C'-shape (IV) or 'V'-shape (V) when a large-magnitude  $B_{xy}$  ( $B_{xy} = 20 \text{ mT}$ ) aligns along the principal axis ( $\alpha = 135^\circ$  and  $315^\circ$ , respectively). The induced pre-stress from the demoulding process may introduce a deviation between the predicted and actual shapes, particularly for (II) and (V). The theoretical  $M_{\text{net}}$  of the robot for each shape is shown on the right. **c**, The clockwise rotation of the 'C'-shaped robot is induced by rotating  $B_{xy}$ . Scale bars, 1 mm.

to produce fluid vortices that propel the robot to the water surface (Fig. 3c, Supplementary Video 1, and Supplementary Fig. 37). Upon emersion, the soft robot strongly pins at the water-air interface by exposing its hydrophobic surface to air.

Inspired by beetle larva that overcome frictionless barriers by performing quasi-static work on liquid-air interfaces<sup>23</sup>, the soft robot

can climb up a water meniscus by deforming into a 'C'-shape to enhance its liquid buoyancy without extra energy expenditure (Fig. 2b, Supplementary Video 2 and Supplementary Information section S7). Upon meniscus climbing and reaching contact with an adjacent solid platform, a slow rotating  $B$  will make the 'C'-shaped robot rotate about its  $z$  axis. The hydrophobicity of its surface allows the robot to be peeled away from the water surface by such rotation (Fig. 2c, Supplementary Video 2 and Supplementary Information section S11B). In contrast to meniscus climbing, the robot can also dive into the liquid bulk by disengaging from the water-air interface via a fast sequence of downward bending, rotation and flipping (Fig. 2d and Supplementary Information section S11A).

In nature, soft-bodied caterpillars use rolling locomotion to escape from their predators, because this is an efficient and fast way to sweep across solid terrains<sup>24</sup>. Like caterpillars, our robots can also roll directionally over a rigid substrate or dive from a solid onto a liquid surface (Figs 2e and 3a). This locomotion is enabled by a high-magnitude rotating  $B$  (such as  $B = 18.5 \text{ mT}$ ), which allows the robot to roll in its 'C'-shape configuration (Supplementary Video 3 and Supplementary Information section S5). However, the curled-up robot cannot roll across substrate gaps wider than its diameter but narrower than the length of the robot; such gaps can instead be traversed by walking.

Walking is a particularly robust way to move over unstructured surfaces and affords precise tuning of stride length and frequency (Fig. 2f, Supplementary Video 3 and Supplementary Information section S6). Inspired by the walking gait of inchworms<sup>25</sup>, the robot can walk in a desired direction when we use a periodic  $B$  to sequentially adapt its tilting angle and curvature. In each walking cycle, the robot first anchors on its front end to tilt forward so that it can pull its back end forward. The robot then anchors on its back end to tilt backwards and extends its front end to achieve a positive stride in a single cycle.

When the walking robot is blocked by narrow openings, it can mimic another caterpillar locomotion<sup>24</sup> and use an undulating gait to crawl through the obstacle (Fig. 2g, Supplementary Video 4 and Supplementary Information section S9). Crawling is encoded by a rotating  $B$  to produce a longitudinal travelling wave that propels the robot along the direction of the wave. A similar control sequence additionally enables the robot to produce an undulating gait to swim efficiently on liquid surfaces<sup>26</sup> (Fig. 3a and Supplementary Video 6). In contrast to crawling, however, the undulating swimming direction is antiparallel with the direction of the travelling waves. Although previous robots with multi-wavelength, harmonic magnetization profiles have also demonstrated undulating swimming locomotion<sup>7</sup>, such robots have not been able to create the critical 'C'- and 'V'-shapes necessary to realize multimodal locomotion.

Like nematodes<sup>27</sup>, the soft robot can jump over obstacles that are too high or too time-consuming to roll or walk over, by imparting an impulsive impact on a rigid surface (Fig. 2h, Supplementary Video 5 and Supplementary Information section S4). The  $B$  control sequence prompts both the robot's rigid-body rotation, which specifies the jumping direction, and elastic deformations to maximize the momentum of its free ends before striking the substrate. This sequence of  $B$  is specified in the robot's local  $y$ - $z$  plane, where  $B_y$  is used for inducing the shape-changing mechanism, whereas the rigid-body rotation of the robot is induced by both  $B_y$  and  $B_z$ .

To illustrate the robot's potential to navigate across unstructured environments (Supplementary Information section S13), we demonstrate that the robot can use a series of locomotion modes to fully explore a hybrid liquid-solid environment (Fig. 3 and Supplementary Video 6) and a surgical human stomach phantom (Fig. 4a, Supplementary Video 7 and Supplementary Information section S14A). Heading towards an *in vivo* ultrasound-guided operation, we also show that the robot can be visualized by an ultrasound medical imaging device as it rolls within the concealed areas of *ex vivo* chicken muscle tissue (Fig. 4b, Supplementary Video 8, Supplementary Information section S14B and Supplementary Fig. 44). The soft robot can additionally

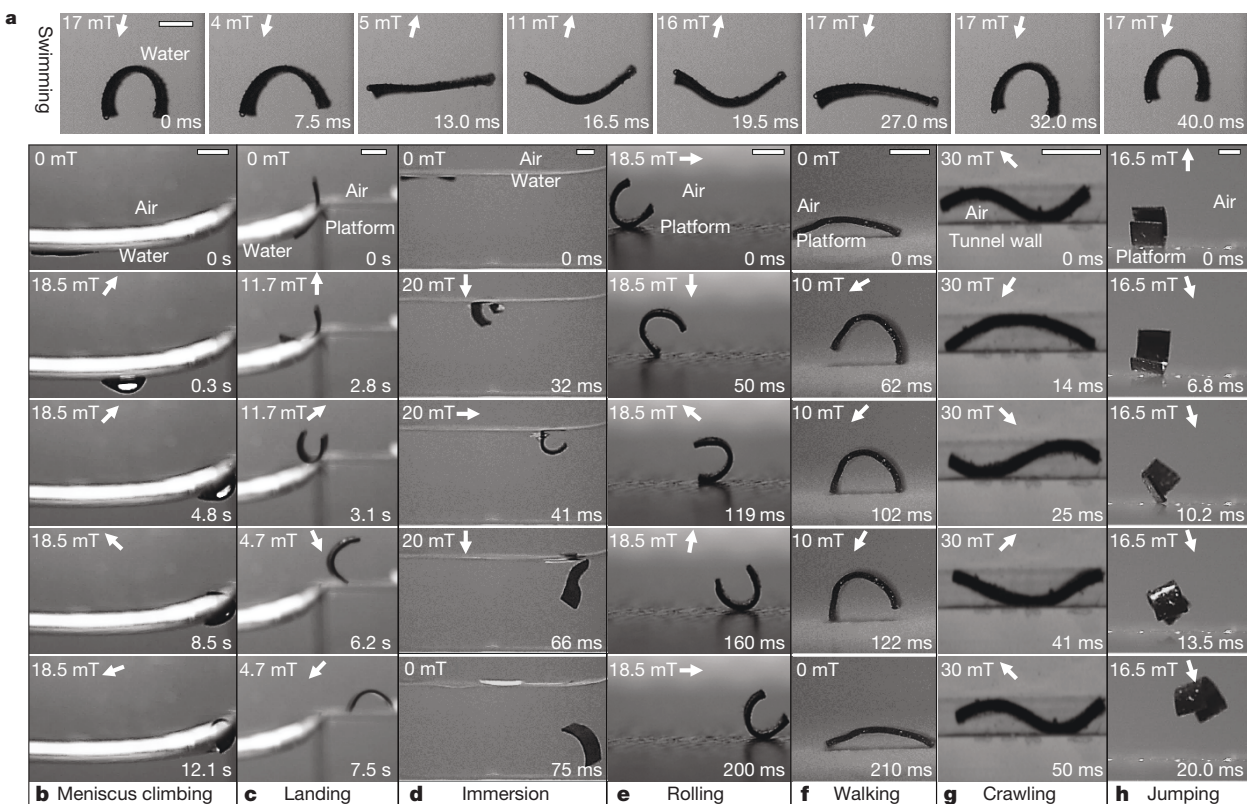


**Figure 2 | Locomotion and transition modes of the soft millirobot.** The sub-panels for the swimming locomotion in **a** are displayed in a horizontal sequence to show the relative vertical displacement between them. The sub-panels for the other types of locomotion are arranged in a vertical sequence to show the relative horizontal displacement between them. The input (**B**) sequences for each locomotion mode are detailed in Supplementary Information sections S4–S11. The corresponding time stamps and **B** in each sub-panel are shown in the bottom-right and top-left corners, respectively. **a**, Jellyfish-like swimming in water using a time-symmetric but speed-asymmetric gait. **b**, Water meniscus climbing. An anticlockwise magnetic torque progressively adapts the pose of the robot as it deforms and ascends owing to buoyancy. **c**, Landing, that is, transition from water surface onto solid ground. A clockwise-rotating **B** peels the robot off the water surface and lets it stand on the platform. **d**, Immersion, that is, transition from the surface into the bulk of a water pool by a combination of curling and rigid-body rotation. **e**, Rolling by a clockwise-rotating **B** of high magnitude. **f**, Walking. The robot tilts and changes its curvature to create a net stride in each cycle. **g**, Crawling inside a tubular channel with a cross-section of  $0.645\text{ mm} \times 2.55\text{ mm}$  by using an undulating travelling wave along the robot's body. **h**, Directional jumping. The robot uses its rigid-body motion and shape change to induce a jumping momentum. More than one robot is used for this illustration but all of these robots have the same design. Scale bars, 1 mm.

transition from water surface onto solid ground. A clockwise-rotating **B** peels the robot off the water surface and lets it stand on the platform. **d**, Immersion, that is, transition from the surface into the bulk of a water pool by a combination of curling and rigid-body rotation. **e**, Rolling by a clockwise-rotating **B** of high magnitude. **f**, Walking. The robot tilts and changes its curvature to create a net stride in each cycle. **g**, Crawling inside a tubular channel with a cross-section of  $0.645\text{ mm} \times 2.55\text{ mm}$  by using an undulating travelling wave along the robot's body. **h**, Directional jumping. The robot uses its rigid-body motion and shape change to induce a jumping momentum. More than one robot is used for this illustration but all of these robots have the same design. Scale bars, 1 mm.

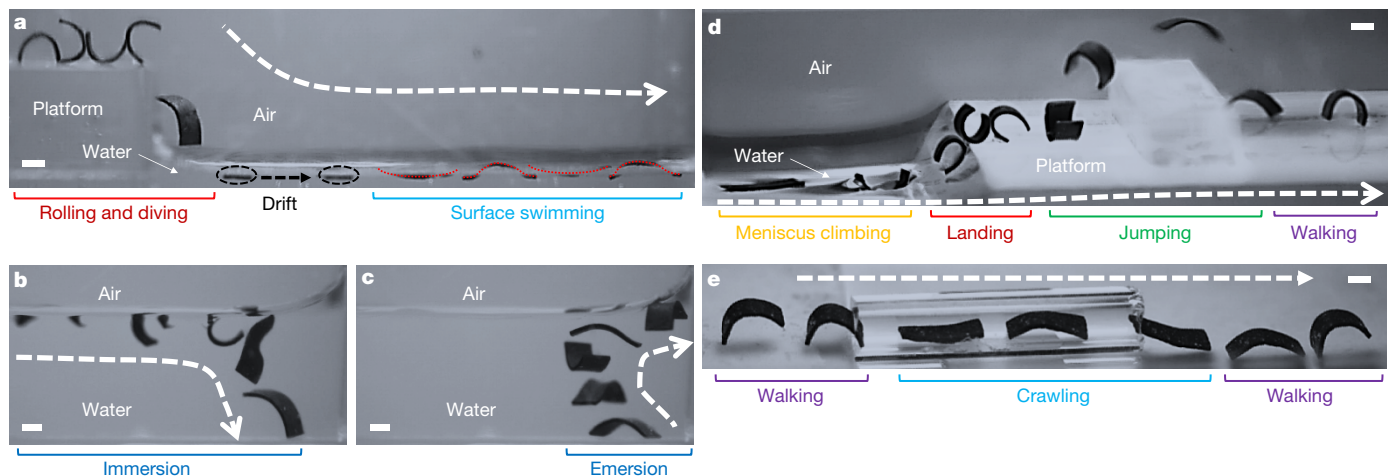


**Figure 3 | Multimodal locomotion over a hybrid liquid–solid environment.** **a**, The soft robot rolls and dives from a solid platform into the adjacent water pool, where it drifts away along the water meniscus. The undulating robot then swims rightwards. **b**, **c**, The robot rotates, disengages from the water surface, sinks, and subsequently swims up from the pool bottom to emerge again at the water–air interface. **d**, The robot climbs up a water meniscus, lands on the solid platform, jumps beyond a

standing obstacle, and walks away. **e**, The robot walks towards a tubular tunnel (diameter 1.62 mm) that impedes its walking gait. The robot then switches to the crawling mode to cross the tunnel, and finally walks away. The locomotion modes were sequentially captured in four separate videos owing to the restrictions of the workspace (Supplementary Information section S2A). Only one robot is used in this illustration. Scale bars, 1 mm.

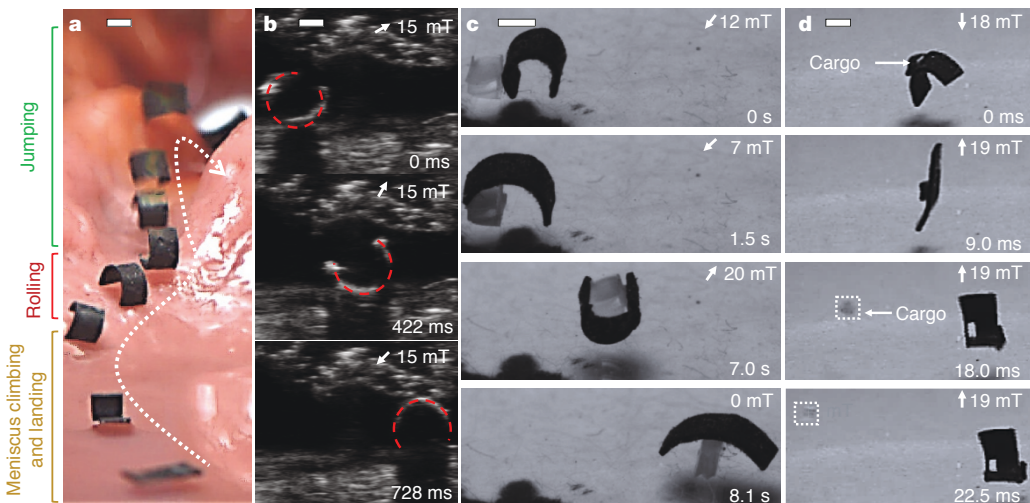


**Figure 4 | Towards medical applications.** **a**, The soft robot navigating across a synthetic stomach phantom using a combination of locomotion modes (Supplementary Video 7). **b**, Ultrasound-guided locomotion: the robot (marked out by dotted red lines) rolls within the concealed areas of an *ex vivo* chicken tissue, as visualized by ultrasound imaging (Supplementary Video 8 and Supplementary Information section S14B). **c**, The robot approaches a cargo item (nylon, 1 mm × 0.8 mm × 1.5 mm) by walking on a flat rigid surface, picks up the cargo by curling into the

accomplish functional tasks like gripping an object and transporting it to a targeted location (Fig. 4c and Supplementary Video 9), as well as ejecting a cargo that is strapped onto the robot (Fig. 4d, Supplementary Video 10 and Supplementary Information section S14C).

In addition to magnetic field-induced torques, magnetic gradient-based pulling forces could also be used to enhance locomotion performance (for example, speed and jumping height). Moving along this direction, we show that the jumping height can be increased by adding magnetic gradient-based pulling forces (Supplementary Video 5), and we will explore other similar possibilities in the future. Using gradient-based pulling exclusively may however be detrimental, as the dynamics of this actuation method is inherently unstable<sup>28</sup>. From a practical standpoint, gradient-based pulling methods are also less energy efficient than locomotion propelled via magnetic field-based torques<sup>29</sup> (Supplementary Information section S15).

The lack of an on-board actuation method prevents the proposed robot from operating in large open spaces, making it unsuitable for outdoor applications such as environment exploration and monitoring. Furthermore, the current demoulding process creates a pre-stress in the magneto-elastic material that induces a small residual curvature in the robot when it is in the rest state (shape I in Fig. 1b and Supplementary Information section S1D). Although the pre-stress does not hinder the robot from achieving multiple modes of locomotion and could be reduced through improved fabrication, it induces small errors in the predicted robot shapes (shapes II and V in Fig. 1b) and partly affects the model matching of the experimental data for the walking and undulating swimming speeds (Supplementary Information sections S6 and S8).

To understand small-scale soft-bodied robot locomotion better, we devised theoretical models to perform a scaling analysis on how the robot's dimensions ( $L$ ,  $w$  and  $h$ , shown in Fig. 1a) would affect the jumping, rolling, walking, meniscus-climbing and undulating swimming locomotion modalities (Supplementary Information sections S4–S8). The theoretical models for the crawling and jellyfish-like swimming locomotion are too difficult to be derived, so we instead used the experimental data in Supplementary Information sections S9–S10 to derive corresponding fitting models. From our theoretical and fitting models, we predict that a larger  $L$  and a smaller  $h$  are always preferred for multimodal locomotion because a longer

'C'-shape, transports away the cargo by rolling and maintaining its 'C'-shape configuration, and releases the cargo by uncurling at a new position (Supplementary Video 9). **d**, Dynamic and selective cargo release (Supplementary Video 10). A paper tissue (0.5 mm × 0.5 mm × 0.1 mm, used as model drug container) is bound to the robot by an extra appendage (Supplementary Information section S14C). After pre-bending the robot, **B** is quickly reversed to open the appendage and release the cargo (cargo highlighted by the white dashed square). Scale bars, 1 mm.

and thinner rectangle shape helps the robot to move faster and jump higher. The models also suggest that  $w$  would affect only the jellyfish-like swimming locomotion and that minimizing  $w$  would increase the swimming speed. There are, however, practical lower bounds for both  $h$  and  $w$ , because our current fabrication technique has difficulties in creating robots that have  $h < 40 \mu\text{m}$  and  $w < 0.3 \text{ mm}$ . Likewise, the practical upper bound of  $L$  is typically constrained by the size requirements of specific applications and the maximum allowable workspace of the electromagnetic coil setup that generates the spatially uniform  $\mathbf{B}$ . A more detailed summary for the scaling analysis and fabrication limits can be found in Supplementary Information section S12.

To validate the theoretical models, we compared them against extensive experimental characterizations conducted across robots with differing dimensions. In general, except for the undulating swimming locomotion, the experimental data agree well with our models (see Supplementary Information sections S4–S8, S12 and Supplementary Table 4). Detailed discussions pertaining to the theoretical and experimental discrepancy for the undulating swimming locomotion can be found in Supplementary Information section S8. These analyses may also provide useful design guidelines for optimizing the performance of future miniature robots that have multimodal locomotion.

We intend to use our robot to study small-scale soft-bodied locomotion on other complex terrains such as within non-Newtonian fluids and on granular media<sup>30</sup>. We also plan to scale down the robots to the sub-millimetre scale and to investigate their potential *in vivo* medical applications.

**Data Availability** All data generated or analysed during this study are included in the published article and its Supplementary Information, and are available from the corresponding author on reasonable request.

Received 19 September; accepted 1 December 2017.

Published online 24 January 2018.

- Chung, S. E., Dong, X. G. & Sitti, M. Three-dimensional heterogeneous assembly of coded microgels using an untethered mobile microgripper. *Lab Chip* **15**, 1667–1676 (2015).
- Ceylan, H., Giltinan, J., Kozielski, K. & Sitti, M. Mobile microrobots for bioengineering applications. *Lab. Chip* **17**, 1705–1724 (2017).

3. Nelson, B. J., Kaliakatsos, I. K. & Abbott, J. J. Microrobots for minimally invasive medicine. *Annu. Rev. Biomed. Eng.* **12**, 55–85 (2010).
4. Sitti, M. et al. Biomedical applications of untethered mobile milli/microrobots. *Proc. IEEE* **103**, 205–224 (2015).
5. Sitti, M. Miniature devices: voyage of the microrobots. *Nature* **458**, 1121–1122 (2009).
6. Sitti, M. *Mobile Microrobotics* (MIT Press, 2017).
7. Diller, E., Zhuang, J., Lum, G. Z., Edwards, M. R. & Sitti, M. Continuously distributed magnetization profile for millimeter-scale elastomeric undulatory swimming. *Appl. Phys. Lett.* **104**, 174101 (2014).
8. Huang, H. W., Sakar, M. S., Petruska, A. J., Pané, S. & Nelson, B. J. Soft micromachines with programmable motility and morphology. *Nat. Commun.* **7**, 12263 (2016).
9. Maeda, S., Hara, Y., Sakai, T., Yoshida, R. & Hashimoto, S. Self-walking gel. *Adv. Mater.* **19**, 3480–3484 (2007).
10. Miyashita, S., Guitron, S., Ludersdorfer, M., Sung, C. R. & Rus, D. An untethered miniature origami robot that self-folds, walks, swims, and degrades. *IEEE Int. Conf. on Robotics and Automation* 1490–1496, <http://ieeexplore.ieee.org/document/7139386/> (Institute of Electrical and Electronics Engineers (IEEE), 2015).
11. Koh, J. S. et al. Jumping on water: surface tension-dominated jumping of water striders and robotic insects. *Science* **349**, 517–521 (2015).
12. Yuk, H., Kim, D., Lee, H., Jo, S. & Shin, J. H. Shape memory alloy-based small crawling robots inspired by *C. elegans*. *Bioinspir. Biomim.* **6**, 046002 (2011).
13. Diller, E. & Sitti, M. Three-dimensional programmable assembly by untethered magnetic robotic micro-grippers. *Adv. Funct. Mater.* **24**, 4397–4404 (2014).
14. Rus, D. & Tolley, M. T. Design, fabrication and control of soft robots. *Nature* **521**, 467–475 (2015).
15. Wehner, M. et al. An integrated design and fabrication strategy for entirely soft, autonomous robots. *Nature* **536**, 451–455 (2016).
16. Lum, G. Z. et al. Shape-programmable magnetic soft matter. *Proc. Natl Acad. Sci. USA* **113**, E6007–E6015 (2016).
17. Aguilar, J. et al. A review on locomotion robophysics: the study of movement at the intersection of robotics, soft matter and dynamical systems. *Rep. Prog. Phys.* **79**, 110001 (2016).
18. Diller, E., Giltinan, J., Lum, G. Z., Ye, Z. & Sitti, M. Six-degree-of-freedom magnetic actuation for wireless microrobotics. *Int. J. Robot. Res.* **35**, 114–128 (2016).
19. Kummer, M. P. et al. OctoMag: an electromagnetic system for 5-DOF wireless micromanipulation. *IEEE Trans. Robot.* **26**, 1006–1017 (2010).
20. Hines, L., Petersen, K., Lum, G. Z. & Sitti, M. Soft actuators for small-scale robotics. *Adv. Mater.* **29**, 1603483 (2017).
21. Amjadi, M., Yoon, Y. J. & Park, I. Ultra-stretchable and skin-mountable strain sensors using carbon nanotubes-Ecoflex nanocomposites. *Nanotechnology* **26**, 375501 (2015).
22. Germell, B. J. et al. Passive energy recapture in jellyfish contributes to propulsive advantage over other metazoans. *Proc. Natl Acad. Sci. USA* **110**, 17904–17909 (2013).
23. Hu, D. L. & Bush, J. W. M. Meniscus-climbing insects. *Nature* **437**, 733–736 (2005).
24. Brackenbury, J. Caterpillar kinematics. *Nature* **390**, 453 (1997).
25. Wang, W. et al. Locomotion of inchworm-inspired robot made of smart soft composite (SSC). *Bioinspir. Biomim.* **9**, 046006 (2014).
26. Taylor, G. Analysis of the swimming of microscopic organisms. *Proc. R. Soc. Lond. Ser. A* **209**, 447–461 (1951).
27. Campbell, J. F. & Kaya, H. K. How and why a parasitic nematode jumps. *Nature* **397**, 485–486 (1999).
28. Zhang, X. D., Mehrtash, M. & Khamesee, M. B. Dual-axial motion control of a magnetic levitation system using Hall-effect sensors. *IEEE/ASME Trans. Mechatron.* **21**, 1129–1139 (2016).
29. Abbott, J. J. et al. How should microrobots swim? *Int. J. Robot. Res.* **28**, 1434–1447 (2009).
30. Aguilar, J. & Goldman, D. I. Robophysical study of jumping dynamics on granular media. *Nat. Phys.* **12**, 278–283 (2016).

**Supplementary Information** is available in the online version of the paper.

**Acknowledgements** W.H. thanks the Alexander von Humboldt Foundation for financial support. This work is funded by the Max Planck Society. We thank Z. Burghard and A. Diem from the University of Stuttgart for evaluating the Young's modulus of our robots, K. Suppel and S. Meyer from Fujifilm Visualsonics for their help with the ultrasound-guided experiments, and the members from Physical Intelligence Department at the Max Planck Institute for Intelligent Systems for their comments.

**Author Contributions** M.S., W.H., G.Z.L. and M.M. proposed and designed the research. W.H. performed all experiments. G.Z.L. developed all theoretical and empirical models, except for the meniscus-climbing model, which was developed by M.M. The experimental data were analysed by W.H., G.Z.L. and M.M. All authors wrote the paper and participated in discussions.

**Author Information** Reprints and permissions information is available at [www.nature.com/reprints](http://www.nature.com/reprints). The authors declare competing financial interests: details are available in the online version of the paper. Readers are welcome to comment on the online version of the paper. Publisher's note: Springer Nature remains neutral with regard to jurisdictional claims in published maps and institutional affiliations. Correspondence and requests for materials should be addressed to M.S. ([sitti@is.mpg.de](mailto:sitti@is.mpg.de)).

**Reviewer Information** *Nature* thanks K.-J. Cho, R. Kramer-Bottiglio and B. Mazzolai for their contribution to the peer review of this work.